Proceedings of Turbo Expo 2011
GT2011
June 6-10, 2011, Vancouver, DC, Canada

GT2011-45954

Mist/air Cooling in a Two-Pass Rectangular Rotating Channel with 45-deg Angled Rib Turbulators

T. S. Dhanasekaran and Ting Wang
Energy Conversion and Conservation Center
University of New Orleans
New Orleans, LA 70148-2220, USA
E-mails: tsdhana@gmail.com; twang@uno.edu

ABSTRACT

Increasing the turbine inlet temperature can increase the gas turbine cycle efficiency. In order to increase the turbine inlet temperature significantly, an advanced cooling system has to be essentially developed. Injection of mist to the coolant fluid is considered a promising technique to protect the hot components such as combustor liners, combustor transition pieces, and turbine vanes and blades. A series of experiments conducted in the past proved the success of mist cooling technology in the laboratory environment. Favorable results from the numerical simulation further encourage continuous exploration of employing mist-cooling technology in the actual gas turbine working environment in various applications. The present study focuses on applying mist cooling to the rotating mist/air internal cooling passage with rib turbulators using numerical simulation.

In the first part, the computational fluid dynamics (CFD) models of smooth and ribbed channels without mist and rotation are validated with the experimental results available in literature. The agreement between the predicted and experimental values in the lower Reynolds number (Re) range is within 3% deviation, and, at higher Re range, the deviation is about 10%. For the smooth channel, the agreement with experimental result is good for the entire range of Re values. In the second part, the rotational effect on the smooth and ribbed channels is predicted and analyzed. In the last part, the mist cooling enhancement on the ribbed channel with rotation is simulated. The secondary flows created due to channel bend and rotation are specifically analyzed. The results show that the mist cooling enhancement is about 30% at the trailing surface and about 20% at the leading surface of the first passage with 2% mist injection. In the second passage, 20% enhancement is predicted for both the surfaces.

NOMENCLATURE

A_p	surface area of droplet
b	slot width (m)
C	concentration (kg/m^3)
D_h	Channel hydraulic diameter
GT	gas turbine
h	convective heat transfer coefficient (W/m^2-K)
H	height of channel (m)
k	turbulent kinetic energy (m^2/s^2)
K	thermophoretic coefficient
Nu	Local Nusselt number, hD_h/kc
m	mass (kg)
q''	wall heat flux (W/m^2)
Re	Reynolds number ($\rho V_j d / \mu$)
Ro	rotational number, $\Omega D_h / V$
T_w	wall temperature (^oC)
V	inlet bulk velocity (m/s)
W	width of channel (m)

Greek

ε	turbulence dissipation (m^2/s^3)
λ	thermal conductivity (W/m-K)
Ω	rotational speed (rad/s)

Subscript

p, d	particle or droplet
r	riblet
s	smooth.

1. INTRODUCTION

Increasing the turbine inlet temperature is one of the major means to increase the gas turbine (GT) efficiency. The increased hot gas temperature typically exceeds the allowable material limit for the blades and vanes. Hence, there is always demand for continuously developing new advanced cooling technologies to cool the hot components in high-performance gas turbines. One of the promising technologies to significantly enhance the heat transfer is to inject water mist into the coolant flow. Each droplet acts as a cooling sink and flies over a distance before it completely vaporizes. This "distributed cooling" characteristic allows controlled cooling by manipulating different sizes of injected water droplets. The mist/steam cooling scheme applicable to an Advanced Turbine System (ATS) was introduced and verified with extensive basic experiments under laboratory working conditions, in a horizontal tube [1,2], a 180-degree curved tube [3], impingement jets on a flat surface [4], and impingement jets on a curved surface [5]. Typically, an average cooling enhancement of 50 - 100% was achieved by injecting 1-3% (wt.) mist into the steam flow. A very high local cooling enhancement of 200 - 300% was observed in the tube and on a flat surface, and local cooling enhancement

above 500% was observed when the steam flow passed the 180-degree bend.

The mist/air film cooling system applied to modern gas turbines was simulated by Li and Wang [6-7] and showed that a small amount of mist injection (2% of the coolant mass flow rate) could increase the adiabatic film cooling effectiveness by about 30%~50% under low temperature, velocity and pressure conditions similar to those in the laboratory. They also investigated the effects of different flow parameters, injection hole configuration, and coolant supply plenum on the cooling effectiveness. In order to simulate the actual GT operating conditions more closely, Li and Wang [8] presented the mist/air film cooling heat transfer coefficient under a conjugate wall condition by employing internal channel cooling beneath the blade surface. The result of conjugated 2-D cases indicated that reverse heat conduction from downstream to upstream along the solid wall was strong within a distance of 5 slot widths. Li and Wang [9] studied the curvature effect on mist film cooling, as well. They found that the magnitude of the mist cooling enhancement was ordered as follows: flat surface > pressure surface > suction surface > leading edge.

Their simulation showed that the film cooling effectiveness increases approximately 40% at the leading edge, 60% on the concave surface, and 30% on the convex surface with 2% mist concentration. Their studies [6-9] on mist/air film cooling were conducted with the turbine in a stationary condition. Recently, Dhanasekaran and Wang [10] simulated the mist/air film cooling enhancement over a rotating blade under gas turbine working conditions with elevated pressure, heat flux, and Reynolds number. They predicted an average of 35% mist cooling enhancement with an equivalent blade surface temperature reduction of 100-125 K.

As a continuation of mist cooling technology developments, the present study employs computational fluid dynamics (CFD) simulations to investigate the cooling performance of applying mist in a gas turbine internal blade with riblets under both stationary and rotating conditions. The early investigations of enhancing turbine airfoil internal cooling under rotating conditions were performed with straight, smooth, circular tubes [11-13]. Han et al. (for example Ref. [14] and [15]) have conducted several experimental studies on straight rib-roughened, non-rotating and rotating channels to investigate the effect of turbulator configurations (such as rib height, spacing and angle), the flow channel aspect ratio, and the flow Reynolds number on the distributions of the local heat transfer and pressure drop. Recently, as CFD schemes became more sophisticated and powerful, numerical studies of heat transfer in ribbed channels have become popular. Chang and Mills [16] employed a low Reynolds number turbulence model for a two-dimensional situation involving flow in a stationary circular tube with repeated rectangular ribs. Arman and Rabas [17] subsequently predicted the flow field and heat transfer in a stationary circular tube with repeated ribs using a two-layer model. Prakash and Zerkle [18] have used the standard k-ε model with wall functions to predict the heat transfer in rotating rib ducts with the assumption of periodic, fully developed flow situations.

In the present study, a mist/air computational model is developed to predict the mist cooling enhancement on the rotating, ribbed, rectangular channel. Initially, the air-only computational model is validated with the experimental results available in open literature. The effects of rotational force on the flow physics and heat transfer in the channel with riblets are investigated. Finally, the mist cooling enhancement is simulated using the validated computational model.

2. Numerical Method

A feasible method to simulate the air/mist flow is to consider the droplets as a discrete phase since the volume fraction of the liquid is small (less than 0.1%) in this study. The trajectories of the dispersed phase (droplets) are calculated by the Lagrangian method. The impacts of the droplets on the continuous phase are considered as source terms to the governing equations of mass, momentum, energy, and species. The continuous phase, including air and water vapor, is formulated with the Eulerian method. The mist cooling computational model has been established and validated within 3% to 15% deviation from the experimental data for various configurations including: mist/steam impingement on a flat surface [19], on a curved surface [20], in a horizontal tube [21], and in a 180 degree bend tube [22]. The detailed description of CFD mist flow modeling is referred to Dhanasekaran and Wang's other studies [19,21] and is not repeated here. A summary of the CFD model is presented below.

Continuous Phase

The time-averaged governing equations of mass, momentum, energy, and species are:

$$\frac{\partial}{\partial x_i}\left(\rho u_i\right) = S_m \tag{1}$$

$$\frac{\partial}{\partial x_i}\left(\rho u_i u_j\right) = \rho \bar{g}_j - \frac{\partial P}{\partial x_j} + \frac{\partial}{\partial x_i}\left(\tau_{ij} - \rho\overline{u'_i u'_j}\right) + F_j \tag{2}$$

$$\frac{\partial}{\partial x_i}\left(\rho c_p u_i T\right) = \frac{\partial}{\partial x_i}\left(\lambda \frac{\partial T}{\partial x_i} - \rho c_p \overline{u'_i T'}\right) + \mu\Phi + S_h \tag{3}$$

$$\frac{\partial}{\partial x_i}\left(\rho u_i C_j\right) = \frac{\partial}{\partial x_i}\left(\rho D_j \frac{\partial C_j}{\partial x_i} - \rho\overline{u'_i C'_j}\right) + S_j \tag{4}$$

where τ_{ij} is the symmetric stress tensor. The source terms (S_m, F_j and S_h) are used to include the contributions from the dispersed phase. $\mu\Phi$ is the viscous dissipation and λ is the thermal conductivity. C_j is the mass fraction of species j in the mixture, and S_j is the source term for this species. D_j is the diffusion coefficient. The diffusion term is used for bi-diffusion between the water vapor and air mass. When the liquid evaporates, the vapor produced surrounds the liquid droplet. Then, this vapor will be transported away through convection and mass diffusion. Three species (oxygen, nitrogen and water vapor) are simulated in the paper.

The terms of $\rho\overline{u'_i u'_j}$, $\rho c_p\overline{u'_i T'}$ and $\rho\overline{u'_i C'_j}$ in the equations above represent the Reynolds stresses, turbulent heat fluxes, and turbulent concentration (or mass) fluxes, which should be modeled properly for a turbulent flow. More detailed investigations and discussions on turbulence models and their effects on the simulation of mist cooling can be found elsewhere [19, 21-23]. The equations for the turbulent kinetic energy (k) and its dissipation rate (ε) are:

$$\frac{\partial}{\partial x_i}\left(\rho u_i k\right) = \frac{\partial}{\partial x_i}\left[\left(\mu + \frac{\mu_t}{\sigma_k}\right)\frac{\partial k}{\partial x_i}\right] + G_k - \rho\varepsilon\,. \tag{5}$$

$$\frac{\partial}{\partial x_i}\left(\rho u_i \varepsilon\right) = \frac{\partial}{\partial x_i}\left[\left(\mu + \frac{\mu_t}{\sigma_\varepsilon}\right)\frac{\partial \varepsilon}{\partial x_i}\right] + C_{1\varepsilon}G_k\frac{\varepsilon}{k} - C_{2\varepsilon}\rho\frac{\varepsilon^2}{k}\,. \tag{6}$$

The term G_k is the generation of turbulence kinetic energy due to the mean velocity gradients. The turbulent viscosity, μ_t, is calculated from the equation:

$$\mu_t = \rho C_\mu \frac{k^2}{\varepsilon} \quad (7)$$

The effective thermal conductivity (λ_{eff}) and the effective diffusion coefficient are calculated by the following two equations, respectively:

$$\lambda_{eff} = \lambda + c_p \mu_t / Pr_t \,, \quad (8)$$

$$D_{eff} = D + \mu_t / Sc_t \,. \quad (9)$$

The constants $C_{1\varepsilon}$, $C_{2\varepsilon}$, C_μ, σ_k, and σ_ε are assigned the following : $C_{1\varepsilon}$= 1.44, $C_{2\varepsilon}$ = 1.92, C_μ = 0.09, σ_k = 1.0, σ_ε=1.3 [24]. In addition, the turbulence Prandtl number, Pr_t, is set to 0.85, and the turbulence Schmidt number, Sc_t, is set to 0.7.

For the near wall region, the enhanced wall treatment is used, in which the standard two-layer model is combined with wall functions. To apply the two-layer approach, the computational domain is separated into a viscosity-affected region and a fully-turbulent region by defining a turbulent Reynolds number, Re_y, which is based on the distance from the wall.

$$Re_y = y k^{1/2} / \nu \quad (10)$$

where k is the turbulence kinetic energy and y is the distance from the wall. The flow is assumed to be in the fully turbulent region if $Re_y > 200$, and the k-ε model is used. Otherwise, the flow is in the viscosity-affected region, and the one-equation model of Wolfstein [25] is used. The turbulent viscosities calculated from the two regions are blended with a blending function (θ) to make the transition smooth.

$$\mu_{t,enhanced} = \theta \mu_t + (1-\theta)\mu_{t,l} \quad (11)$$

where μ_t is the viscosity from the k-ε model of high Reynolds number, and $\mu_{t,l}$ is the viscosity from the near-wall one-equation model. The blending function is defined so it is 0 at the wall and 1 in the fully-turbulent region. The wall functions are also enhanced by blending linear (laminar) and logarithmic (turbulent) laws-of-the-wall to make the blended wall function applicable throughout the entire near-wall region.

Discrete Phase

Based on Newton's 2nd law, the droplet motion can be formulated by

$$m_p d\mathbf{v_p}/dt = \sum \mathbf{F} \quad (11)$$

where $\mathbf{v_p}$ is the droplet velocity (vector). The right-hand side is the combined force acting on the droplet, which normally includes the hydrodynamic drag, gravity, and other forces such as Saffman's lift force, the thermophoretic and Brownian forces, etc. In this study, Saffman's lift force is included.

To include radiation heat transfer, the P1 model [26] was used. The P1 model determines the local radiation intensity by solving the transport equation for incident radiation, G as follows:

$$\nabla \cdot (\Psi \nabla G) - a\,G + 4a\sigma T^4 = S_g \quad (12)$$

where $\Psi = 1/(3(a+\sigma_s) - (C\sigma_s))$, a = absorption coefficient, σ_s = scattering coefficient, σ = Stefan-Boltzmann constant, S_g = radiation source, C = linear-anisotropic phase function.

The heat source due to radiation in the following form is directly substituted into the energy equation.

$$-\nabla \cdot q_r = 4a\sigma T^4 \quad (13)$$

The droplet's heat transfer is given in the following equation. $m_p c_p \frac{dT}{dt} = A_p h(T_\infty - T) + \frac{dm_p}{dt} h_{fg} + A_p \varepsilon_p \sigma\left(\theta_R{}^4 - T^4\right)$ (14)

where h_{fg} is the latent heat, ε_p = particle emissivity, θ_R = radiation temperature. The convective heat transfer coefficient (h) can be obtained with an empirical correlation [27 and 28]:

$$Nu_d = \frac{hd}{\lambda} = 2.0 + 0.6\,Re_d^{0.5}\,Pr^{0.33} \quad (15)$$

where Nu_d is the Nusselt number, and Pr is the Prandtl number.

The mass change rate or vaporization rate in Eq. (14) is governed by concentration difference between droplet surface and the air stream,

$$-\frac{dm_p}{dt} = \pi d^2 k_c (C_s - C_\infty) \quad (16)$$

where k_c is the mass transfer coefficient, and C_s is the vapor concentration at the droplet surface, which is evaluated by assuming the flow over the surface is saturated. C_∞ is the vapor concentration of the bulk flow, and is obtained by solving the species transport equations. The values of k_c can be given from a correlation similar to Eq. (17).

$$Sh_p = \frac{k_c d}{D} = 2.0 + 0.6 Re_p^{0.5} Sc^{0.33} \quad (17)$$

where Sh is the Sherwood number, Sc is the Schmidt number (defined as ν/D), and D is the diffusion coefficient of vapor in the bulk flow.

When the droplet temperature reaches the boiling point, the following equation (18) can be used to evaluate its evaporation rate:

$$-\frac{dm_p}{dt} = \pi d^2 \left(\frac{\lambda}{d}\right)(2.0 + 0.46 Re_p^{0.5}) \ln\left(1 + c_p(T_\infty - T)/h_{fg}\right)/c_p \quad (18)$$

where λ is the gas/air heat conductivity and c_p is the specific heat of the bulk flow.

Theoretically, evaporation can occur at two stages: (a) when the temperature is higher than the saturation temperature (based on local water vapor concentration), water evaporates, and the evaporation is controlled by the water vapor partial pressure until 100% relative humidity is achieved; (b) when the boiling temperature (determined by the air-water mixture pressure) is reached, water continues to evaporate.

The stochastic method [26] is used to consider the turbulence dispersion effect on droplet tracking. The droplet trajectories are calculated with the instantaneous flow velocity ($\bar{u} + u'$), and the velocity fluctuations are then given as:

$$u' = \varsigma\left(\overline{u'^2}\right)^{0.5} = \varsigma(2k/3)^{0.5} \quad (19)$$

where ς is a normally distributed random number. This velocity will apply during the characteristic lifetime of the eddy (t_e), a time scale calculated from the turbulence kinetic energy and dissipation rate. After this time period, the instantaneous velocity will be updated with a new ς value until a full trajectory is obtained.

To consider the interactions between the tiny liquid droplets around the riblets and the effect of the rotation and channel bend, the Taylor Analogy Breakup (TAB) model [29] and O'Rourke coalescence model [30] are employed in this

study. The TAB model is a classic method based upon Taylor's analogy between an oscillating and distorting droplet and a spring mass system, where the surface tension forces, droplet drag force and droplet viscosity forces are analogized with restoring, external, and damping forces. O'Rourke's coalescence model considers coalescence as an outcome of collision. O'Rourke's algorithm assumes that two droplets may collide only if they are in the same continuous-phase cell. This assumption can prevent droplets that are quite close to each other but not in the same cell from colliding, although the effect of this error is lessened by allowing some droplets that are farther apart to collide. The overall accuracy of the scheme is second-order in space. Once it is determined that two particles collide, the outcome of the collision is "coalescence" if the droplets collide head on, and "bouncing" if the collision is more oblique. Droplet breakup and coalescence models improve discrete phase calculation when strong local acceleration or deceleration is present in the flow field such as over the riblet surface or around the channel bend with rotation.

2.1 Boundary Conditions

2.1.1 Airflow

The approach adopted in this study is to first validate the CFD model for air-only flows with experimental results available in open literature, and then to simulate the air/mist flow in order to predict the cooling enhancement. The experimental results of Fu et al. [31] are used for this purpose. The geometry of a two-pass channel with a 45-deg ribbed wall considered for this study is shown in Fig. 1a. The dimensions are exactly the same as used in the experimental study [31]. The channel cross section is 12.7 x 12.7 mm making the aspect ratio of 1:1 (W:H) throughout the length except the bend portion. The rib height, e = 1.59 mm, the channel hydraulic diameter, D_h = 12.7 mm, and the rib pitch-to-height ratio, p/e = 10. Each pass has a 152.4 mm long heating section (Fig. 1a). The computational domain contains a 111.13 mm unheated entrance length to provide the fully-developed flow condition. The clearance of the 180-deg sharp turn is 12.7 mm from tip to end wall. The divider wall has a thickness of 19.1 mm with a 9.53 mm radius at the tip. The ribs with a cross section of 1.59 mm × 1.59 mm are placed on the top and bottom of the channel. As in the experimental set-up, a gap of 0.79 mm is maintained between the ribs and the sidewall. The ratio of rib pitch-to-rib height is 10. The air inflows with Reynolds numbers of 5,000, 10,000, 25,000, and 40,000 with a temperature of 300 K and the rotational speed of 550 rpm are considered. The constant heat flux of 4,800 W/m^2 is assigned to the heating portion of the computational domain.

A turbulence intensity of 1% is assigned at the mainstream inlet. The pressure at the flow exit is assumed to be maintained at a constant value of 1 atm. All of the walls in the computational domain are adiabatic and have a no-slip velocity boundary condition.

2.1.2 Droplet injection

A uniform droplet size of 5μm is considered, then the effect of distributed droplet diameters is simulated for comparison. The mass ratio of liquid droplets over airflow is 2% (about 1.1 x 10^{-4} kg/s for mist) for both cases. The number of mist injection points at the coolant inlet depends on the number of computational meshes at the inlet surface. In the present case, about 500 injection points are placed. The trajectory number for stochastic tracking is chosen to be 15 for each injection. The boundary condition of droplets at the walls is assigned as "reflect," meaning the droplets elastically rebound off once reaching the wall. Details about the model are documented in a previous study by Dhanasekaran and Wang [21]. At the outlet, the droplets just simply escape from the computational domain.

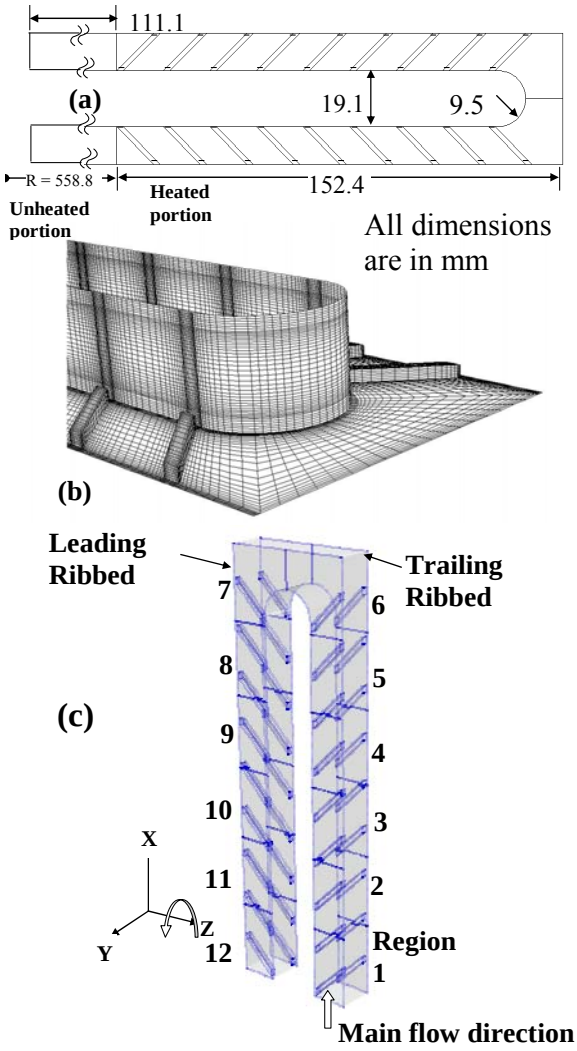

Figure 1 (a) Plane view of the channel geometry (b) computational elements on the surfaces and (c) 3-D schematics and coordinates, modeled following experimental work of "Fu et al. [31].

2.2 Meshing and simulation procedure

The computational domain is constructed by structured hexahedral elements as shown in Fig. 1b. More intensive meshes are used near the wall and ribbed area. A total of 1 million cells are used for this configuration. In the rotating channel case, the coordinate system shown in Fig. 1c rotates with the channel. In this system, the flow is steady, but the centrifugal and Coriolis forces are accounted for via the additional source terms in the equation of motion (Eq.2). The droplets will be affected by the rotating effect indirectly because the droplet traces are attached to the coordinates of the continuous phase. Therefore, there is no need to add the centrifugal force in the force balance equation (Eq. 11). The computation is carried out using the commercial CFD software FLUENT (Version 6.2.16) from Ansys, Inc. The simulation uses the segregated solver that employs an implicit pressure-correction scheme and decouples the momentum and energy equations. The SIMPLE algorithm is used to couple the pressure and velocity. A second order upwind scheme is selected for spatial discretization of the convective terms and

species. The computation is conducted for the continuous phase (air) first. After obtaining an approximate converged flow field of the air, the dispersed phase of droplet trajectories are calculated. At the same time, drag, heat and mass transfer between the droplets and the air are calculated. Variable property values are calculated using polynomial equations for air and a piecewise approximation for water droplets. The mixture properties are calculated by the mass-weighted method. It was discovered that the property databases for water vapor and steam in FLUENT are not sufficient. A detailed database has been incorporated through the use of a Function statement.

Iterations proceed alternately between the continuous and discrete phases. Ten iterations in the continuous phase are conducted for every two iterations in the discrete phase. Converged results are obtained after the mass residual reaches 10^{-4}, the energy residual reaches 10^{-6}, and the momentum and turbulence kinetic energy residuals reach 10^{-5} each. These residuals are the summation of the imbalance for each cell. The computation was carried out in parallel processing on two dual-core Pentium clusters with 10 nodes and 6 nodes, respectively.

3. RESULTS AND DISCUSSION

3.1 Validation of CFD Model

The computational model for air-only flow is validated against the experimental results of Fu et al. [31]. The grid independence study is carried out with mesh sizes of 0.5 million, 1 million, and 1.5 million cells using the standard k-ε turbulence model. Fig. 2 shows the Nussult number distribution for inlet flow conditions for Re = 5,000, 10,000, 25,000 and 40,000. The Nu plotted here are averaged values from the leading and trailing ribbed walls. The heat transfer coefficient (h) and Nusselt number are calculated as follows:

$$h = q''/(T_w - T_{b,x}) \quad (20)$$

$$Nu = hD_h/\lambda \quad (21)$$

Where T_w is the wall temperature, $T_{b,x}$ is the bulk temperature at the x location, and λ is the thermal conductivity of the coolant.

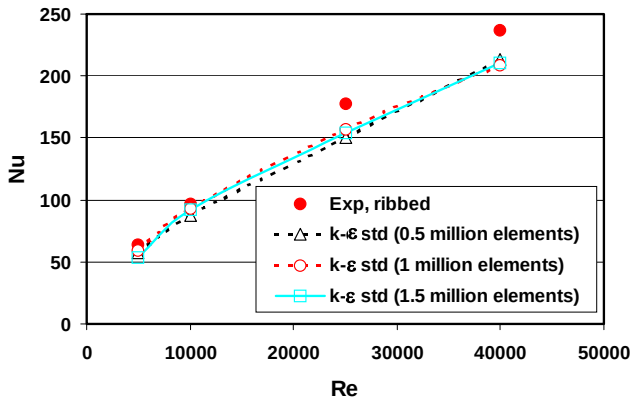

Figure 2 Grid independence analysis

In general, the predicted result does not vary too much for the three different mesh numbers, and specifically, the result of 1 million elements almost coincides with that of 1.5 million meshes. Therefore, the rest of computational analysis is conducted with 1 million meshes. The prediction is about 3% lower than the experimental result in the lower Reynolds number range and about 10% lower in the higher Reynolds number range.

To improve the accuracy of the computational model, apart from the standard k-ε turbulence model, the other four turbulence models including RNG k-ε, Realizable k-ε, standard k-ω, and the Reynolds Stress Model (RSM) are employed for comparison, and the results are shown in Fig. 3. The predicted results from all the models are almost the same for the lower Re numbers and vary within ± 10% at the higher Re numbers. Comparatively, the standard k-ε model provides the closest match with the experimental results; therefore, the standard k-ε model with enhanced-wall function is employed for cases in this study.

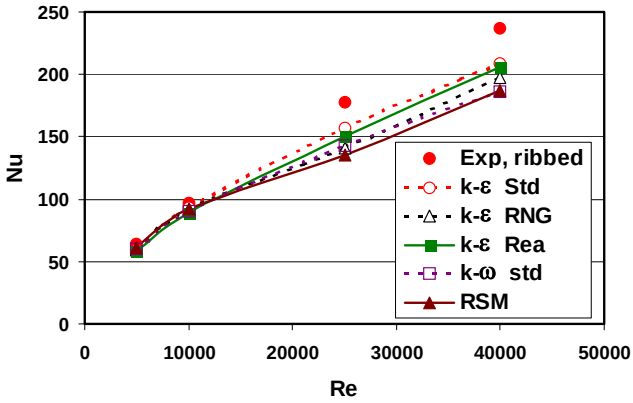

Figure 3 Effect of five turbulence models on Nu distribution in a smooth channel.

The comparisons between the CFD and the experimental data of both the ribbed and smooth channels are shown in Fig. 4. The agreement of the Nusselt numbers is very good for the entire Re range for the smooth channel. It clearly shows that the flow becomes complex with riblets, and, in the high Re range, the CFD model's accuracy drops noticeably.

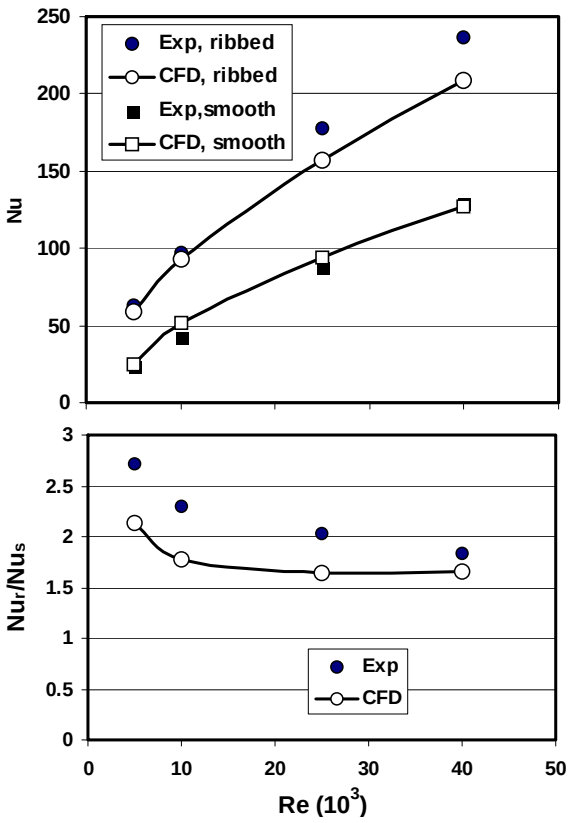

Figure 4 CFD Model validation (k-ε model).

Figure 4b shows the heat transfer enhancement (Nu_r/Nu_s) due to riblets. Nu for riblets and smooth surfaces are

individually calculated using Eq. 17. Higher heat transfer enhancements are seen at low Re values. An average of about 12% under-prediction of the enhancement ratio (Nu_r/Nu_s) is noticed for this simulation with a higher local deviation of 20% at a low Re, but a lower local deviation of 8% at a high Re. This trend of error is the opposite of the actual Nusselt number prediction due to the sensitivity of the cooling enhancement ratio calculation. For example, at Re = 5,000, the Nusselt numbers are 8% off for the smooth channel and 6.4% for the ribbed channel, but the ratio of Nu_r/Nu_s gives a higher percentage deviation of 21%.

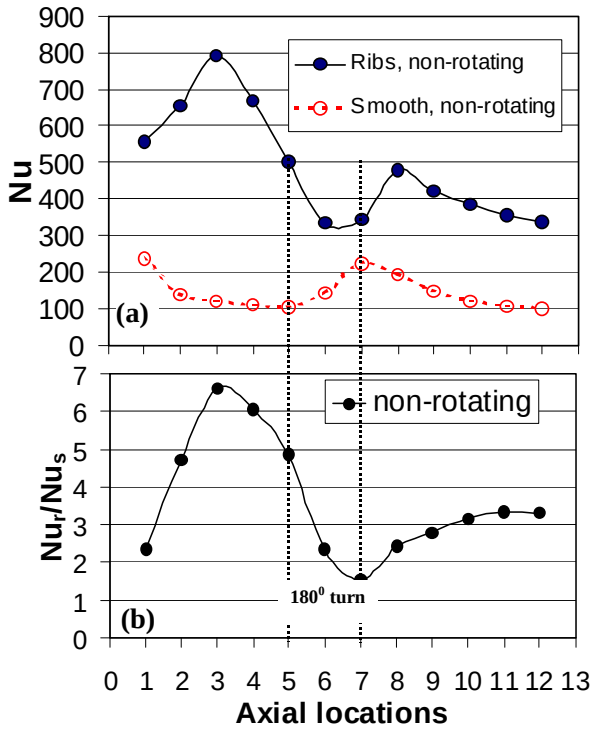

Figure 5 Effect of riblets on peripheral averaged Nusselt number at Re = 25,000 without rotation

3.2 The Effect of Rotation on Smooth and Ribbed Channels with Air-only Flow

To investigate the effect of riblets over a smooth surface on the heat transfer enhancement under non-rotating conditions, the Nusselt number distributions are plotted in Fig. 5. The Nu values are regionally averaged throughout the heated section for Re = 25,000. The location of each region is shown in Fig. 1c. The Nu distributions over the leading and trailing edges are similar without rotation, so only the averaged Nu values over the leading surface is shown in Fig. 5 to simplify the analysis. In the actual measurement, there were slight deviations between these surfaces at the second pass, which was observed by Fu et al. [31]. In the smooth channel, the Nu value decreases once the flow enters the channel, but increases in the bend section to a maximum value at the end of bend. With riblets, the Nu value increases to a maximum value at location 3 and reaches a local maximum downstream of the bend. The Nusselt number ratio distribution in Fig. 5b clearly shows the heat transfer enhancement with ribs at various axial locations. The flow physics responsible for this heat transfer pattern will be discussed in the later sections. Please note that no local heat transfer data is available from Fu et al. [31], so no experimental data is shown in Fig. 5.

The effects due to the rotation on smooth and ribbed channels are investigated and explained in Fig. 6. Without rotation, the Nu distribution along the streamwise direction on leading and trailing surfaces is almost the same for smooth and ribbed channels. In the first pass, with rotation on the smooth channel, Fig. 6a shows that the Nu values increase on the trailing surface compared to the non-rotational case and decrease on the leading surface. The trend is reversed in the second pass, i.e., Nu values increase at the leading surface and decrease at the trailing edge. On the other hand, Fig. 6b shows that the effect of rotation on the ribbed surface is mainly captured in the first pass. In the second pass, the effect is comparatively minimal. The experimental results [31] showed the same effect and confirmed the accuracy of predicting the correct trend of the rotating effect of the present simulation.

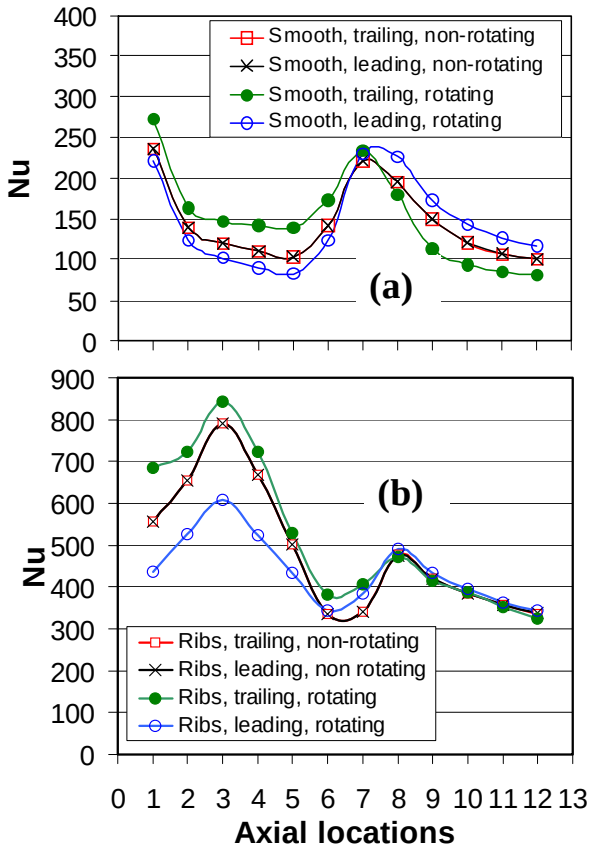

Figure 6 Effects of rotation on (a) smooth and (b) ribbed channels at Re=25,000.

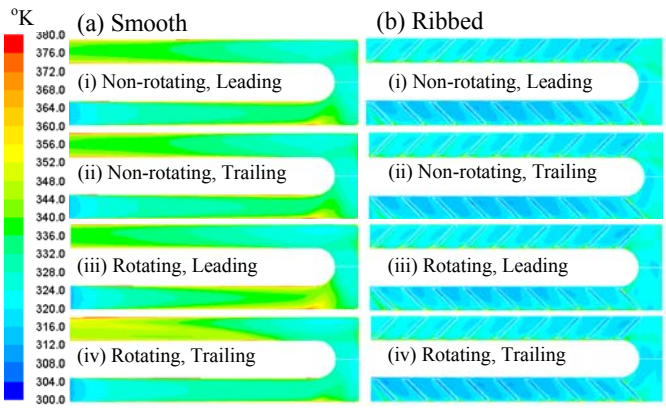

Figure 7 Temperature contours at leading and trailing surfaces (Re = 25,000)

Figure 7 shows the local temperature distributions, which consistently reflect the Nusselt results in Fig. 6, indicating that lower temperature areas correspond to higher cooling rates and, thus, higher Nusselt numbers.

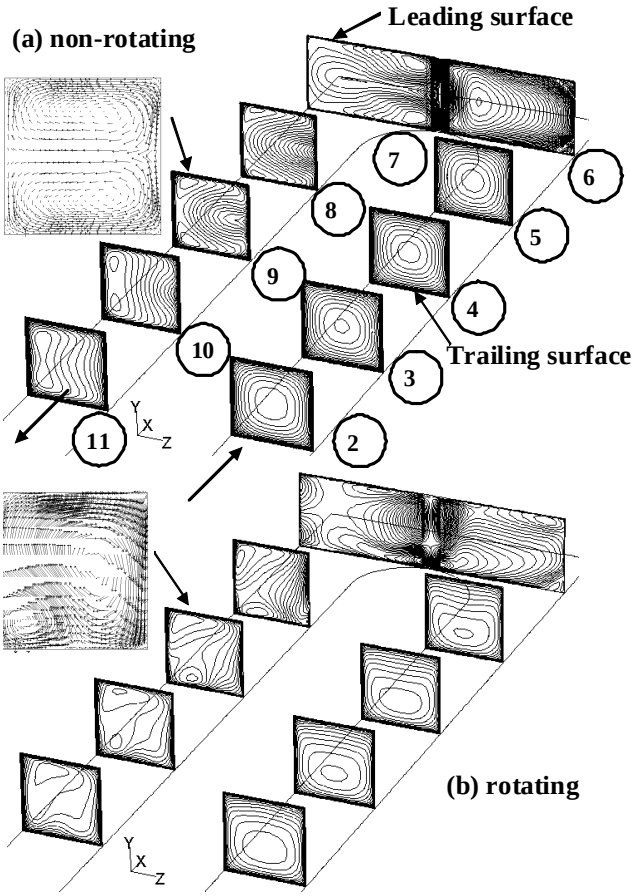

Figure 8 Velocity contours at selected cross-sections of smooth channel with and without rotation at Re = 25,000. Rotation is in the positive z-direction or out of the paper.

To explain the flow physics, the velocity contours at selected normal cross-sections in the first and second passes for both the rotating and non-rotating cases are shown in Fig. 8. It is clearly seen from Fig. 8a that the core flow is located at the midsection of the channel for the non-rotating case. For the rotating case (Fig. 8b), the core flow is pushed toward the trailing surface by the Coriolis force ($-\boldsymbol{\omega} \times \mathbf{V}$) right from the axial location 1, imposing a higher velocity gradient, and, hence, a higher heat transfer on the trailing surface. In the second pass, the flow is almost symmetric with an organized secondary flow moving from the inner surface toward the outer surface without rotation (Fig. 8a). However, in the rotating case, the core flow turns toward the leading edge due to the Coriolis force. The maximum heat transfer takes place immediately after the bend near region 8 for all conditions and surfaces; implying that the heat transfer enhancement is not caused by rotation. Rather, it is dominated by the flow behavior induced by the channel bend. The inserted cross-sectional flow vector plot at station 9 in Fig.8a for the non-rotating case shows formation of the secondary flow as the counter rotating vortices under the influence of centrifugal force induced by the channel bend. In the rotating case (Fig. 8b), this pair of counter-rotating vortices are interfered with by the Coriolis force. The top vortex grows and the the bottom vortex diminishes as shown in the inserted cross-sectional flow field at Station 9 of Fig. 8b. More upwelling flow can be seen moving toward the leading surface. This results in higher heat transfer on the leading surface in the second pass as shown in Fig. 6a. There are several papers (for example Al-Qahtani et al. [32]) explaining the flow structure of rotating channels with various aspect ratios of channel width over height and rotational numbers.

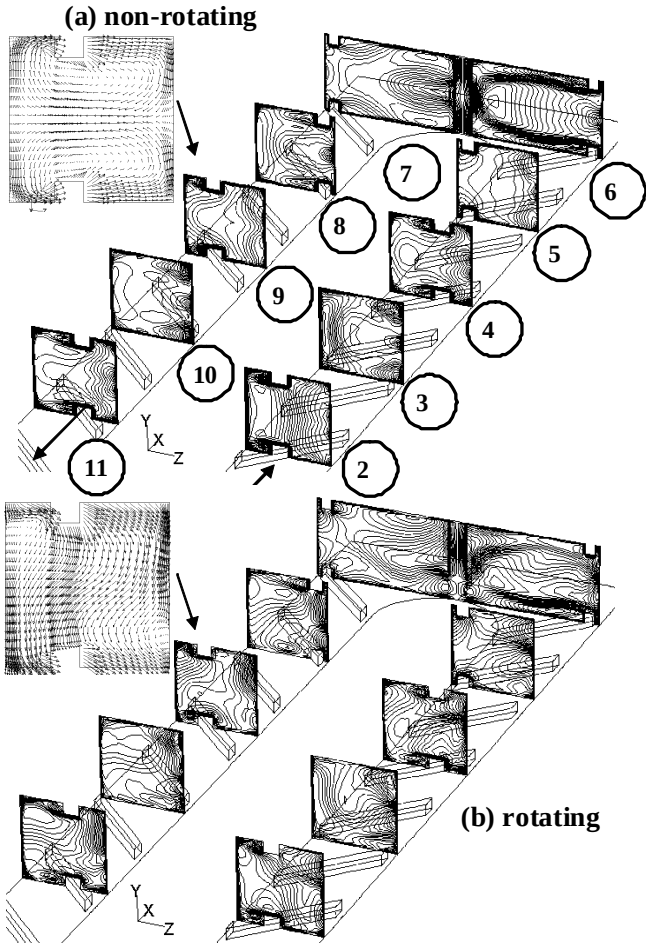

Figure 9 Velocity contours at selected lateral cross sections of ribbed channel with and without rotation (Re = 25,000).

The velocity contour plot for the ribbed case (Fig. 9) shows more complex flow fields. It is interesting to see that the large structure of the secondary flow consisting of a pair of counter-rotating vortices is still visible, but the vortices only locally disturbed by the riblets in second pass of the non-rotating channel. Similar to the situation in the rotating smooth channel, the core flow of the rotating ribbed channel is pushed and imposed upon the trailing edge in the first pass by the Coriolis force. But, different from the rotating smooth channel, the counter-rotating vortices disappear in the second pass for the rotating ribbed channel case.

Figure 10 shows the velocity vector plots on the vertical mid-plane in the ribbed channel for both non-rotating and rotating cases.

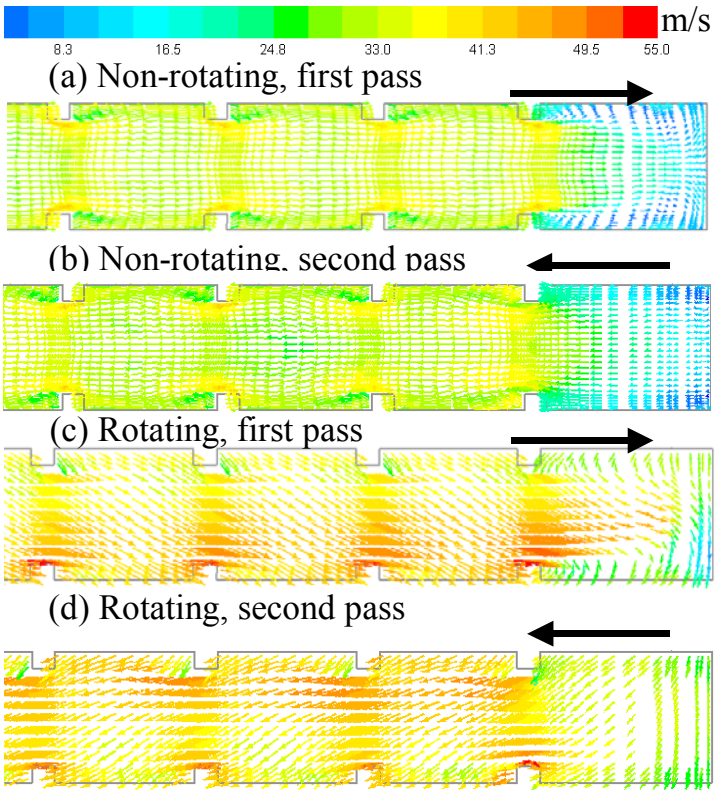

Figure 10 Velocity vector plot at normal cross section of ribbed channel in the first and second passes (Re = 25,000).

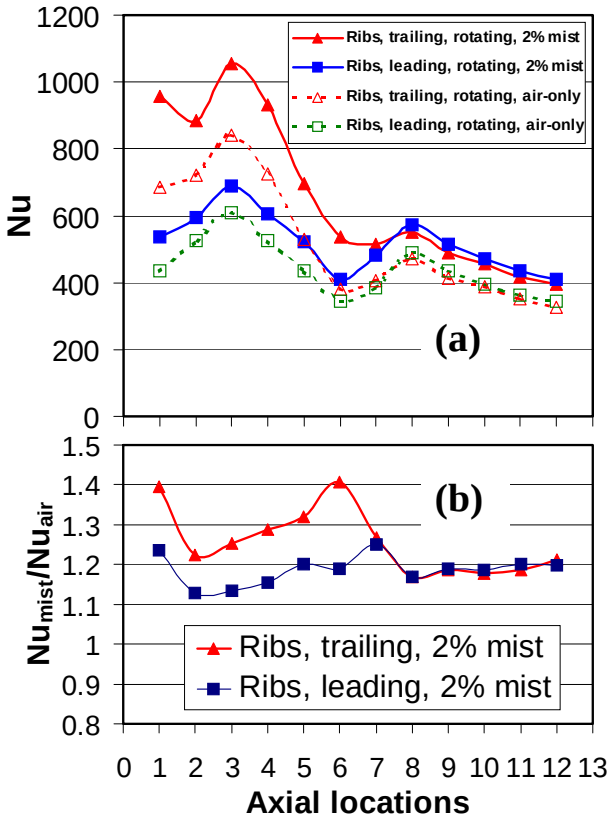

Figure 11 Mist cooling enhancement on ribbed channel at Re = 25,000.

3.3 Mist/air cooling enhancement with rotation on Ribbed Channels

To predict the mist/air cooling enhancement, 2% mist (1.1 x 10^{-4} kg/s) was injected at the inlet of the ribbed channel. The uniform 5 micron diameter droplets are considered initially to investigate the droplet size variation and droplet dynamics. The droplet breakup and coalescence are found to have a negligible effect on this study. A typical heat transfer result predicted for Re = 25,000 is shown in Fig. 11. In general, the mist cooling achieves a higher Nu value in the first pass than in the second pass due to the rotational effect. In the first pass, mist cooling enhancement on the trailing surface is higher than that on the leading surface. In the second pass, the cooling enhancement is almost the same for both the surfaces. It can be noted that in the entry region (region 1, Fig. 11a) of the trailing surface, the heat transfer is very high compared to the air-only case. In the first pass, the average mist cooling enhancement ratio is about 30% on the trailing surface and about 20% on the leading surface. In the second pass, a relatively uniform, 20% cooling enhancement ratio is predicted for both of the surfaces. Figure 12 shows the droplet traces in the rotating ribbed channel. Some droplets move with spiral paths, suggesting that the droplets are subject to the effect of centrifugal and Coriolis forces. Figure 13 shows the liquid droplet concentration (kg/m^3) distributions on three cut-away planes with one near the leading surface, one near the trailing surface, and one in the center of the channel. It is interesting to see more liquid concentration near the upstream surface of each riblet and low liquid concentration behind the riblet, indicating accumulation of liquid droplets when they hit the riblet surface. No clear correlation can be drawn between the liquid concentration level in Fig. 13 and the heat transfer level in Fig. 7.

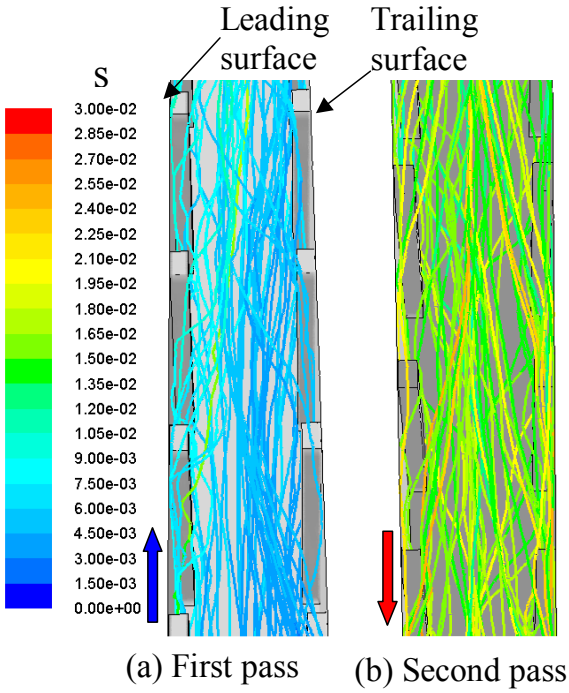

Figure 12 Droplet traces colored by residence time in the vicinity of rib gaps for rotating case at Re = 25,000.

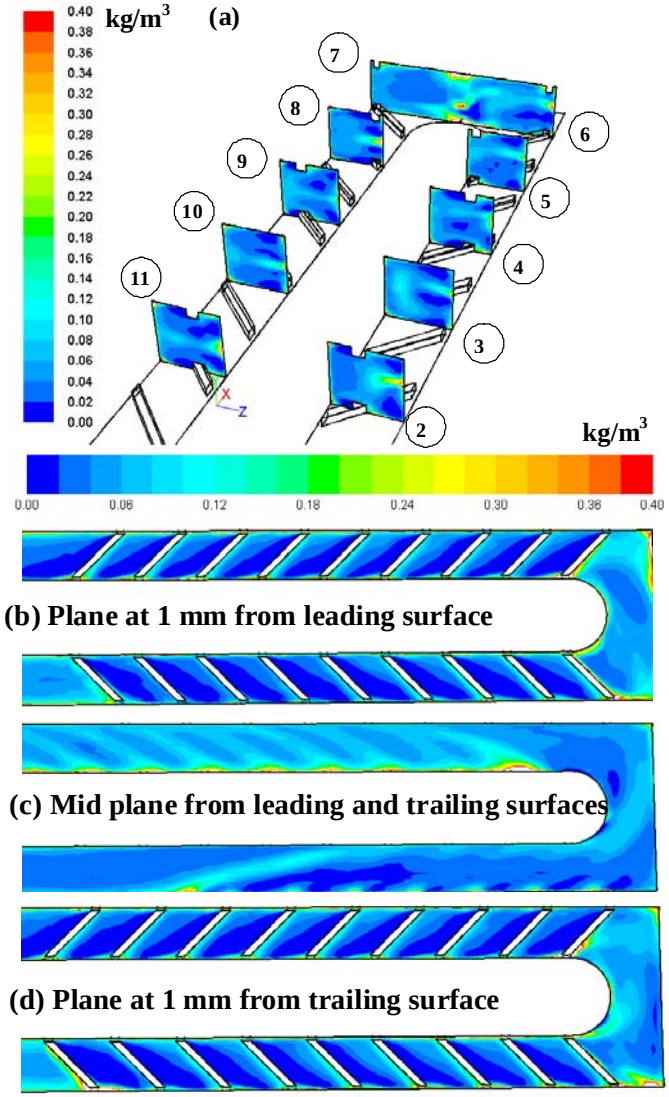

Figure 13 Liquid concentration at various planes for rotating riblet case at Re = 25,000.

To simulate the actual non-uniform distribution of liquid droplet sizes more closely, the Rosin-Rammler distribution function is used based on the assumption that an exponential relationship exits between the droplet diameter, d_d, and the mass fraction of droplets with diameter greater than d. This relationship is expressed in the following equation:

$$Y_d = e^{-(d/d_m)^n} \quad (22)$$

where d_m refers to the mean diameter (5μm) and n refers to the spread parameter. From the relationship, the spread parameter (2.4) is calculated and used to fit the experimental size distribution of Guo et al [3] into the CFD model.

The difference between using the uniform 5μm droplets and non-uniform droplets can only be observed in the entrance region of the channel, as shown in Fig. 14. This can be explained by the fast evaporation of droplets smaller than 5μm in the case with distributed droplets in the entrance region. The impact to downstream heat transfer is negligible. More details about droplet distribution can be found in Dhanasekaran and Wang's study [21].

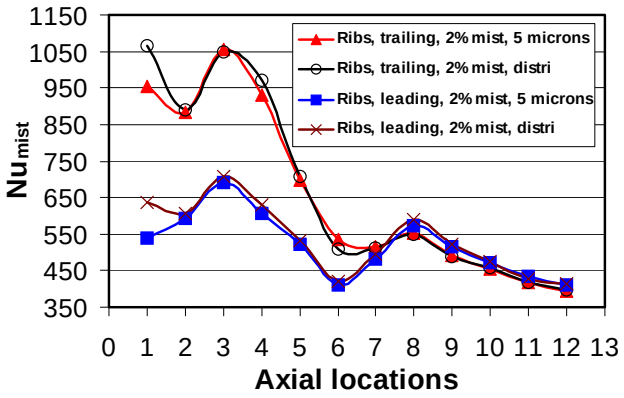

Figure 14 Effect of droplet distribution.

4. CONCLUSIONS

A CFD model was developed to predict mist/air cooling enhancement in a rotating ribbed rectangular channel. The results are concluded below:

- The CFD model for air-only flow on a ribbed channel was validated with the experimental results and achieved good agreement at lower Re values. At higher Re values, the deviation is about 10%. For the smooth channel, the agreement is within 3% for the entire range of Re values.
- For the smooth channel, rotation imposes centrifugal force upon the trailing surface in the first pass and enhances its cooling; whereas in the second pass, the Coriolis force pushes the flow toward the leading surface and results in more effective cooling on the leading surface.
- For the ribbed channel, the effect of rotation is only realized in the first pass with enhanced cooling on the trailing surface and suppressed cooling on the leading surface. The effect of the rotation in the second pass is negligible.
- With 2% (wt.) mist injection, the average mist cooling enhancement is about 30% on the trailing surface and about 20% on the leading surface in the first pass under rotating conditions. In the second pass, about 20% mist cooling enhancement is predicted for both the surfaces.
- When subjected to the centrifugal and Coriolis forces, some of the water droplets are seen to move in spiral paths. More liquid concentration is seen on the upstream surface of riblets and much lower liquid concentration behind the riblet.

ACKNOWLEDGMENTS

This study was supported by the Louisiana Governor's Energy Initiative via the Clean Power and Energy Research Consortium (CPERC) and administered by the Louisiana Board of Regents.

5. REFERENCES

[1] Guo, T., Wang, T., and Gaddis, J. L., 2000, "Mist/Steam Cooling in a Heated Horizontal Tube: Part 1: Experimental System," ASME J. Turbomachinery, 122, pp. 360-365.

[2] Guo, T., Wang, T., and Gaddis, J.L., 2000, "Mist/Steam Cooling in a Heated Horizontal Tube: Part 2: Results and Modelling," ASME J. Turbomachinery, 122, pp. 366-374.

[3] Guo, T., Wang, T., and Gaddis, J. L., 2000, "Mist/Steam Cooling in a 180-Degree Tube," ASME J. Heat Transfer, 122, pp. 749-756.
[4] Li, X., Gaddis, T., and Wang, T., 2001, "Mist/Steam Heat Transfer of Confined Slot Jet Impingement," ASME J. Turbomachinery, 123, pp. 161-167.
[5] Li, X., Gaddis, T., and Wang, T., 2003, "Mist/Steam Heat Transfer with Jet Impingement onto a Concave Surface," ASME J. Heat Transfer, 125, pp. 438-446.
[6] Li, X. and Wang, T., 2005, "Simulation of Film Cooling Enhancement with Mist Injection", *ASME Journal of Heat Transfer*, Vol. **128** (6), pp.509-519.
[7] Li, X., and Wang, T, 2007, " Effects of Various Modellings on Mist Film Cooling", *ASME Journal of Heat Transfer*, Vol. 129, pp. 472-482.
[8] Li, X., and Wang, T., 2008, "Two-Phase Flow Simulation of Mist Film Cooling on Turbine Blades with Conjugate Internal Cooling", *ASME Journal of Heat Transfer*, Vol. **130**, pp.102901/1-8.
[9] Li, X. and Wang, T., 2008, "Computational Analysis of Surface Curvature Effect on Mist Film Cooling Performance" ASME Journal of Heat Transfer, vol. 130, pp. 121901/1-9
[10] Dhanasekaran, T. S., and Wang, T., 2009, "Simulation of Mist Film Cooling on Rotating Gas Turbine Blades", *ASME Turbo Expo* 2009 (GT2009-59424), Orlando, Florida.
[11] Mori, Y., Fukada, T., and Nakayama, W., 1971, "Convective Heat Transfer in a Rotating Circular Pipe (2nd Report)," Int. J. Heat Mass Transfer, 14, pp. 1807–1824.
[12] Metzger, D. E., and Stan, R. L., 1977, "Entry Region Heat Transfer in Rotating Radial Tubes," AAIA Paper No. 77-189.
[13] Morris, W. D., and Ayhan, T., 1979, "Observations on the Influence of Rotation On Heat Transfer in the Cooling Channels of Gas Turbine Rotor Blades," Proc. Inst. Mech. Eng., 193, pp. 303–311.
[14] Han, J. C., 1984, "Heat Transfer and Friction in Channels with Two Opposite Rib-Roughened Walls", ASME J. Heat Transfer, Vol. 106, pp.774-781.
[15] Han, J. C., Chandra, P. R., and Lau, S. C., 1988, "Local Heat/Mass Transfer Distributions Around Sharp 180^o Turns in Two-Pass Smooth and Rib-Roughened Channels," ASME J. Heat Transfer, Vol. 110, No. 1, pp. 91-98.
[16] Chang, B. H., and Mills, A. F., 1991, "Application of a Low-Reynolds Number Turbulence Model to Flow in a Tube With Repeated Rectangular Rib Roughness," PHONICS Journal, vol. 4, No. 3, 1991, pp. 262-288.
[17] Arman, B., and Rabas, T., 1992, "The influence of the Prantdl Number on the Thermal Performance of Tubes With the Separation and Reattachment Mechanism," Enhanced Heat Transfer, ASME HTD-Vol. 202, 1992, pp.77-88.
[18] Prakash, C., Zerkle, R., 1995, "Prediction of Turbulent Flow and Heat Transfer in a Ribbed Rectangular Duct With and Without Rotation," ASME J. Turbomahcinery, Vol. 117, 1992, pp.77-88.
[19] Wang, T. and Dhanasekaran, T. S., 2010, "Calibration of CFD Model for Mist/Steam Impinging Jets Cooling," ASME Journal of Heat Transfer, in print. (Modified from Paper GT2008-50737, Turbo Expo2008, Berlin, Germany, June 9-13, 2008).
[20] Wang, T. and Dhanasekaran, T. S., 2011, "Model Verification and Prediction of Mist/Steam Cooling with Jet Impingement Onto a Concave Surface," ASME Journal of Turbomachineary, in print.
[21] Dhanasekaran, T. S. and Wang., 2008, "Validation of Mist/steam Cooling CFD Model in a Horizontal Tube," ASME paper HT2008-56280, Summer Heat Transfer Conference, Jacksonville, Florida, August 10-14, 2008.
[22] Dhanasekaran, T. S. and Wang., 2010, "CFD Model Validation and Prediction of Mist/Steam Cooling in a 180-Degree Bend Tubes," Proceedings of International Heat Transfer Conference, IHTC-2010-22833, August 8-13, 2010, Washington, DC, USA.
[23] Li, X., Gaddis, J. L., and Wang, T., 2001, "Mist/steam Heat Transfer in Confined Slot Jet Impingement," *ASME J. Turbomachinery*, Vol. **123**, pp. 161-167.
[24] Launder, B. E. and Spalding, D. B.,1972, "Lectures in Mathematical Models of Turbulence", Academic Press, London, England.
[25] Wolfstein, M., 1969, "The Velocity and Temperature Distribution of One-dimensional Flow with Turbulence Augmentation and Pressure Gradient", *Int. J. Heat Mass Transfer,* Vol. 12, pp. 301-318.
[26] Fluent Manual, Version 6.2.16, 2005, Fluent, Inc.
[27] Ranz, W. E., and Marshall, W. R. Jr., 1952, "Evaporation From Drops, Part I," Chem. Eng. Prof., 48, pp. 141-146.
[28] Ranz, W. E., and Marshall, W. R. Jr., 1952, "Evaporation From Drops, Part II," Chem. Eng. Prof., 48, pp. 173-180.
[29] O'Rourke, P. J. and Amsden, A. A., 1987, "The Tab Method for Numerical Calculation of Spray Droplet Breakup," SAE Technical Paper 872089, 1987.
[30] O'Rourke, P. J., 1981, "Collective Drop Effects on Vaporizing Liquid Sprays," PhD dissertation, Princeton University, New Jersey, 1981.23.
[31] Fu, W. L., Wright, L. M., Han, J. C., 2006, "Rotational Buoyancy Effects on Heat Transfer in Five Different Aspect-Ratio Rectangular Channels With Smooth Walls and 45 Degree Ribbed Walls", ASME J. Heat Transfer, Vol. 128, pp.1130-1141.
[32] Al-Qahtani, M., Chen, H. C., and Han J.C., 2003, "A Numerical Study of Flow and Heat Transfer in Rotating Rectangular channels (AR = 4) with 45 deg Rib Turbulators by Reynolds Stress Turbulence Model," ASME J. Heat Transfer, Vol. 125, pp. 19-26.